




# Highly customized 1010 nm, ns-pulsed Yb-doped fiber amplifier as a key tool for on-demand single-photon generation

OLIVER DE VRIES,<sup>1,\*</sup> MARCO PLÖTNER,<sup>1</sup> FLORIAN CHRISTALLER,<sup>2</sup> HAO ZHANG,<sup>2,3,4</sup> ANNIKA BELZ,<sup>2</sup> BENJAMIN HEINRICH,<sup>2</sup> HARALD KÜBLER,<sup>2</sup> ROBERT LÖW,<sup>2</sup> TILMAN PFAU,<sup>2</sup> TILL WALBAUM,<sup>1</sup> THOMAS SCHREIBER,<sup>1</sup>  AND ANDREAS TÜNNERMANN<sup>1</sup>

<sup>1</sup>Fraunhofer Institute for Applied Optics and Precision Engineering IOF, Albert-Einstein-Strasse 7, 07745 Jena, Germany

<sup>2</sup>Physikalisches Institut and Center for Integrated Quantum Science and Technology, Universität Stuttgart, Pfaffenwaldring 57, 70569 Stuttgart, Germany

<sup>3</sup>State Key Laboratory of Quantum Optics and Quantum Optics Devices, Institute of Laser Spectroscopy, Shanxi University, Taiyuan 030006, China

<sup>4</sup>Collaborative Innovation Center of Extreme Optics, Shanxi University, Taiyuan 030006, China

\*oliver.devries@iof.fraunhofer.de

**Abstract:** The development of highly customized technical devices is a decisive feature of technically complex setups, as frequently observed in quantum experiments. This paper describes the development and realization of an Yb-doped all-fiber amplifier system designed for such a special application, more specifically, an on-demand single-photon source based on four-wave mixing with rubidium Rydberg atoms. The laser is capable of generating bandwidth-limited configurable nanosecond pulses up to peak powers of  $>100$  W and with pulse repetition frequencies (PRF) between 50 Hz and 1 MHz at selectable wavelengths (1008–1024 nm). Especially the amplification of the 1010 nm reference seed at the lower edge of the amplification range for Yb-based fibers is challenging and tends to produce amplified spontaneous emission (ASE) at higher wavelengths. To achieve high ASE suppression, particularly at low pulse repetition frequencies, two acousto-optical modulators (AOM) are utilized both for pulse picking and for temporal filtering. The synchronization between pulse repetition frequency and AOM driver signal allows pulse amplitude fluctuations to be kept below 1%, while ASE is suppressed by at least 85 dB (PRF = 1 MHz) and 65 dB (PRF = 1 kHz).

© 2020 Optical Society of America under the terms of the [OSA Open Access Publishing Agreement](#)

## 1. Introduction

Almost 40 years ago, the idea of a universal quantum computer emerged and it was soon assumed that specific quantum algorithms could surpass conventional computers [1,2]. Just recently, Google reported on an experiment claiming quantum supremacy for the first time [3] setting a landmark in the field of quantum computing. Although not everybody agrees on the size of this milestone or the estimated time scales for classical computation (including rival IBM), it nevertheless shows the high potential of quantum speed-up [4].

Beside controlling qubits and quantum logic gates with microwaves [5], quantum computation can also be realized with an all-optical approach using linear optical elements, specifically beam splitters and phase shifters [6,7]. For this type of quantum architectures photo detectors, on-demand single-photon sources and quantum repeaters are essential building blocks. They can also provide e.g. ancillary photons to enable the heralding of successful quantum gate operations [8,9]. Ideally, these sources should be reliable and, if possible, working robustly under basic lab environmental conditions, preferably at room temperature. Nowadays, there is a multitude of

suitable solid-state host materials reported on to emit single photons [10], some of those even at room temperature [11–13]. However, the use of solid materials makes these sources prone to phonon interaction, spin noise, strain and drifting electric fields. Typically, even under optimal conditions, spectral dispersion in an array of such solid state based sources prevents order of magnitude scaling. Alternatively, heralded single photons can also be obtained from a transient coherent spin excitation of the ground state in a hot atomic vapor cell instead [14]. Sources based on atomic transitions in alkali vapors are also particularly well suited for subsequent storage in quantum memories (based on the same atoms) as required e.g. in quantum repeater protocols [15].

Recently, a single-photon on-demand approach for a photon source based on an atomic transition has been followed using a reservoir of rubidium atoms in a wedged micro glass cell [16]. By exploiting strong Rydberg interactions in a hot atomic vapor via a laser driven four-wave mixing scheme, the authors emphasize major advantages for future applications like robust operation at room temperature, scalability and integrability. Despite the tempting prospects, some features of this setup need to be reviewed. Firstly, the nanosecond-pulsed lasers used for controlled excitation and deexcitation operate at a practically too low pulse repetition frequency (PRF = 50 Hz). Secondly, pulse-to-pulse amplitude fluctuations and pulse jitter issues have to be minimized. Thirdly, by using a different set of laser wavelengths, a more efficient Rydberg excitation scheme can be addressed, which, due to larger dipole matrix elements, allows a stronger coupling between the intermediate and Rydberg states and therefore less laser power is required. This newly designed second-generation experiment also defines the very special characteristics of the required laser systems that no general-purpose laser can fulfill.

In this paper we discuss the challenges in developing these specialized laser systems, which will be used as key tools in a revised version of the single-photon generation experiment based on Ref. [16]. Taking a closer look to the very often complex nature of experiments in the emerging scientific branch of quantum technology, in many cases there is an immanent need for highly customized equipment. Moreover, this report can be seen as a blueprint for the useful interplay between the difficulties of quantum experiments and the degree of customization of the instruments available to address them.

## 2. Deriving application-driven laser specifications

The demand for these specialized lasers is the result of the following simulation for the next generation single-photon source, which is based on a rubidium-filled micro-cell [16]. The simulation shows that it is efficient to excite a rubidium-Rydberg state with the optical wavelengths 421.67 nm (transition 1–2) and 1010.6 nm (transition 2–3). With a third laser at 1018.6 nm (transition 3–4), the four-wave mixing process can be used to create photons at 420.3 nm (transition 4–1). The four-wave mixing scheme with the involved rubidium energy levels is shown in Fig. 1(a). The brightness of this kind of single-photon source was measured in [16] to be around 4%.

A key value is the coupling strength between the energy levels in the atom, which is given by the dipole matrix elements. Compared to the previous experiment [16], the excitation scheme presented here has twice the coupling strength between the intermediate and the Rydberg state ( $6P_{1/2}$  to  $40S_{1/2}$ ).

An excitation volume about the size of the Rydberg blockade sphere suppresses multiple excitations [17]. Residual multiple excitations in a blockade volume dephase quickly due to the strong Rydberg-Rydberg interaction. The emission of such dephased states occurs in the full solid angle, resulting in a preferred single-photon emission in forward direction [18,19]. As this type of single-photon source is operated at a temperature of 160°C, the Rydberg excitation must be on the nanosecond time scale to be in the quasi-frozen gas regime, which is the reason for

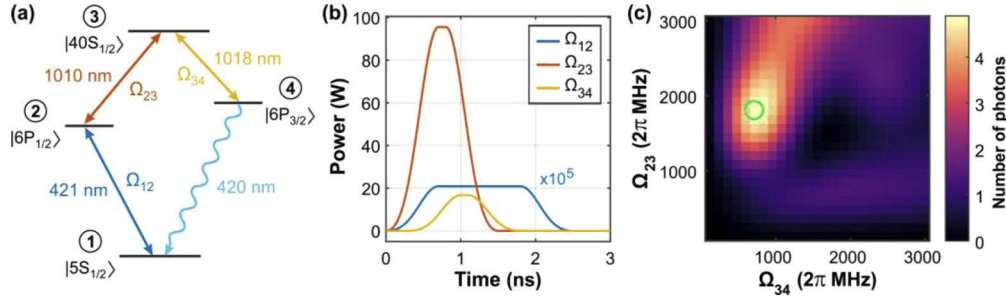


**Fig. 1.** (a) Four-wave mixing level scheme. The excitation path is clockwise from the  $6P_{1/2}$  to  $6P_{3/2}$  via  $40S_{1/2}$ . The laser detuning for all transitions has been set to zero while the coupling between levels is given by the Rabi frequencies  $\Omega$ . (b) Optimized pulse sequence. Since the waists of the lasers are defined (details in text), the powers of the excitation pulses are plotted for the optimized Rabi frequencies. For illustration, the power of the first excitation pulse (blue) is multiplied by  $10^5$ . (c) Number of generated 420 nm photons as a function of the Rabi frequencies of Rydberg excitation and deexcitation with a green circle marking the optimum. The optimized Rabi frequencies have the values  $\Omega_{12} = 2\pi \cdot 1340$  MHz (not shown),  $\Omega_{23} = 2\pi \cdot 1800$  MHz and  $\Omega_{34} = 2\pi \cdot 720$  MHz. The simulation does not include the Rydberg blockade, which ideally limits the emission to one photon.

using nanosecond-pulsed lasers. The bandwidth of the excitation pulses is Fourier-limited to some 100 MHz, which also determines the bandwidth of the emitted photons.

The following calculation for a single atom shows how the parameters for the four-wave mixing process can be optimized.

The atom-light interaction is described by the master equation in Lindblad form [20],

$$\frac{\partial \rho(t)}{\partial t} = -\frac{i}{\hbar} [H, \rho] + L_D(\rho(t)), \quad (1)$$

which is solved numerically to obtain the time-dependent density matrix  $\rho(t)$  of the atomic state, where  $\hbar$  is the reduced Planck constant,  $H$  is the Hamiltonian and  $L_D$  is the Lindblad operator. The Lindblad operator for our system has the form,

$$L_D(\rho) = \sum_{\{i \rightarrow f\}} \Gamma_{i \rightarrow f} \left( |f\rangle \rho_{ii} \langle f| - \frac{1}{2} \{ |i\rangle \langle i|, \rho \} \right), \quad (2)$$

where  $\Gamma$  is the decay rate,  $|i\rangle$  is the initial state and  $|f\rangle$  is the final state. The Hamiltonian for a four-level systems is given by,

$$H = \hbar \begin{pmatrix} 0 & \frac{\Omega_{12}}{2} & 0 & 0 \\ \frac{\Omega_{12}^*}{2} & \delta_{12} & \frac{\Omega_{23}}{2} & 0 \\ 0 & \frac{\Omega_{23}^*}{2} & \delta_{23} & \frac{\Omega_{34}}{2} \\ 0 & 0 & \frac{\Omega_{34}^*}{2} & \delta_{34} \end{pmatrix},$$

with the Rabi frequency  $\Omega$ , describing the coupling, and the detuning  $\delta$  between the light and the energy level. Furthermore, the Doppler effect is included in the simulation by solving the master equation for different velocity classes (detuning  $\delta \propto v$ ) and calculating the weighted mean value according to the Boltzmann distribution. For the here presented simulation the laser detuning was set to zero. In addition to the natural decay of energy levels, the polariton decay is also considered in the simulation, assuming a polariton lifetime of  $\tau_{\text{Polariton}} = 1.2$  ns [21].

From the obtained value for the coherence  $\rho_{14}$  the generated electric field  $E_{14}$  and respectively the intensity or number of generated photons  $N$

$$N(t_0) = \frac{1}{2} \frac{\omega_{14}}{\hbar \varepsilon_0 c} n^2 |d_{14}|^2 L^2 A \int_0^{t_0} |\rho_{14}(t)|^2 dt \quad (4)$$

can be calculated. Here  $\varepsilon_0$  stands for the vacuum permittivity,  $c$  for the speed of light,  $\omega_{14}$  for the angular frequency of the transition,  $n$  for the atomic density,  $d_{14}$  for the dipole matrix element of the according transition,  $L$  for the length of the cell and  $A$  for the illuminated cross section. For this derivation, the slowly varying envelope approximation was presumed, and it was assumed that the density matrix elements do not depend on the position inside the cell or the illuminated cross section. To maximize the number of generated photons in a fixed cell ( $L = 1 \mu\text{m}$ ,  $A = \pi(0.5 \times 10^{-6})^2 \text{ m}^2$ ) with a steady atomic density ( $n = 1.4 \times 10^{21} \text{ m}^{-3}$ ) and a time  $t_0 = 10 \text{ ns}$  the term  $\int_0^{t_0} |\rho_{14}(t)|^2 dt$  must be maximized. For this purpose, not only the Rabi frequencies for the three lasers, but also their pulse lengths and relative delays to each other were varied [22].

For the pulse shape of all three pulses, a Blackman-like pulse is assumed, whereby the peak value is held constant for a certain period of time. The obtained ideal pulse sequence can be seen in Fig. 1(b). Pulse 1–2 (blue) and 2–3 (orange) start at the same time, while pulse 3–4 (yellow) is delayed by 0.3 ns. The essential parameters for the realization of the experiment are the Rabi frequencies for the Rydberg transitions, therefore ideal values can be found when the number of photons is maximized, see Fig. 1(c). Note that the simulation does not include the nonlinearity of the Rydberg blockade effect. From the maximization it can be concluded that for the first excitation a laser with a beam waist of  $0.5 \mu\text{m}$  and a peak power of  $209 \mu\text{W}$  is necessary to achieve a Rabi frequency of  $\Omega_{12} = 2\pi \cdot 1340 \text{ MHz}$ . To excite the atoms into the Rydberg state with a Rabi frequency of  $\Omega_{23} = 2\pi \cdot 1800 \text{ MHz}$  a laser with a beam waist of  $35 \mu\text{m}$  and a peak power of  $96 \text{ W}$  is required. For the third transition a value of  $\Omega_{34} = 2\pi \cdot 720 \text{ MHz}$  was determined for the Rabi frequency, which corresponds to a laser with a beam waist of  $35 \mu\text{m}$  and a peak power of  $17 \text{ W}$ .

With the experience gained from previous experiments and the implementation of this new scheme, a number of generalized requirements for the lasers can be formulated:

- Addressable wavelengths between 1008–1024 nm (discrete values that potentially address further Rydberg states, reference 1010.6 nm)
- Adjustable pulse peak power  $>100 \text{ W}$  (at all PRF)
- PRF from 50 Hz to 1 MHz (maintaining constant peak power)
- Flexible pulse duration between 0.5–10 ns (reference 1 ns)
- Pulse duration jitter  $<100 \text{ ps}$
- Pulse-to-pulse peak power fluctuation  $<1\%$  (standard deviation)
- ASE suppression  $>60 \text{ dB}$  (reference at PRF = 1 kHz)
- Bandwidth-limited pulses
- Maintaining central frequency and bandwidth over amplification and pulse picking process
- Stable polarization with PER  $>20 \text{ dB}$ , thus only PM fibers are used for the amplifiers and for passive components

Commercially available lasers cannot meet such a complex set of specifications.

### 3. Fiber amplifier design

At first glance, the requirements seem to limit the options how to set up the lasers. Since bandwidth-limited pulses are required at very flexible pulse repetition frequencies, power levels etc., a fundamental master-oscillator power-amplifier design is mandatory. As master oscillator a continuous-wave, single-frequency and tunable laser diode can be used. In this case, the pulses must be shaped by a subsequent intensity modulator, resulting in pulse peak powers of only a few milliwatts. As a consequence, the amplifier system requires a very high gain, not only to achieve the specified pulse peak power, but also to overcome the total losses of the system. Rare earth-doped glass fibers are known as high-gain solid state amplifier architectures, especially when it comes to high PRFs with comparatively low pulse energies [23–25]. By doping the core with ytterbium ions, a broad spectral amplification range between 1000–1100 nm can be covered. However, sufficient amplification at the lower edge of the Yb-doped glass emission cross section can only be achieved by a high population inversion in the fiber-core and a comparatively high seed power [26]. Direct fiber core pumping produces the required degree of population inversion, with seed power management being a matter of amplifier design. Questions about the type and number of preamplifiers as well as losses due to other optical elements play a decisive role. In order to repeatedly attenuate the strong formation of amplified spontaneous emission (ASE) near the 1030 nm (highest gain) spectral region, both temporal and spectral filtering measures must be carried out. The design resulting from these considerations is shown schematically in Fig. 2.

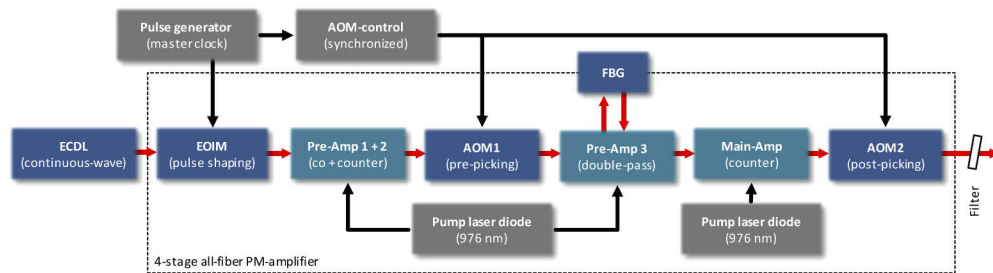


**Fig. 2.** Schematic representation of the all-fiber PM-amplifier setup (ECDL: External-Cavity Diode Laser; EOIM: Electro-Optical Intensity Modulator; AOM: Acousto-Optical Modulator; FBG: Fiber Bragg-Grating; PM: Polarization-Maintaining).

The seed source is a 100 mW fiber-coupled continuous-wave frequency-stabilized external cavity diode laser with 100 kHz line width. By passing an electro-optical intensity modulator (EOIM) a 3 MHz pulse train is shaped with a bandwidth-limited optical spectrum. The limited EOIM on/off contrast of ~25 dB causes low-power background radiation to transmit through the component. With a pulse duration of 1 ns, the resulting emission thus contains ~50% continuous-wave portion (later suppressed by the AOMs). However, the seed power at this point is sufficient for the first (co-pumped) preamplifier, whose output immediately serves as input for the (counter-pumped) second amplifier. The pulse pre-picking process at AOM1 reduces the repetition frequency by factor 3–30 down to 1 MHz–100 kHz leaving appropriate power for the next two amplifier stages, the (double-pass) third preamplifier and the (counter-pumped) main-amplifier. AOM2 pulse post-picking further reduces the repetition frequency while keeping the pulse peak power constant.

Since the seed conditions along the amplification path are constantly changing, the next question is how the individual amplifier fibers can be optimally designed in terms of fiber length. In order to answer this, a simulation was carried out using a complete model based on the rate equation taking ASE into account [27]. Under the assumption of a realistic pump power and a worst-case seed power influenced by the PRF and losses of optical components, splices etc., the



performance of all four fiber amplifiers was investigated with regard to average output power and residual pump power by varying the total fiber length, see Fig. 3. The modeled fiber is a projection of commercially available polarization-maintaining single-clad fibers and has a 976 nm pump absorption of 80 dB/m and a mode field diameter of 6  $\mu\text{m}$ .

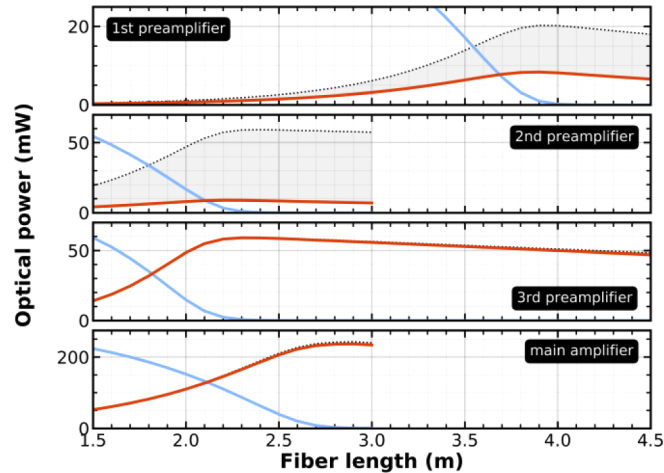


**Fig. 3.** Simulation of all four amplifier stages showing optical powers (y-axis), when the amplification of a fiber with a particular length (x-axis) is simulated. The different optical powers are: 1010.6 nm signal power (red), spectrally integrated total power (black dotted), ASE-related radiation content (gray area) and residual 976 nm pump power (blue).

The three preamplifier stages share a common (triple split) 976 nm pump laser diode, whereby 100 mW is launched into each fiber core. The first preamplifier is set up in co-pump configuration, which ensures low-noise amplification of the initially weak post-EOIM 30  $\mu\text{W}$  seed signal. Although a lot of non-signal light is generated, sufficient 1010.6 nm emission is available, which reaches its peak when a 3.9 m long fiber is chosen (Fig. 3, upper plot). At this fiber length, most pump light is absorbed. The use of even longer fibers results in fiber segments with low inversion reabsorbing the signal light in turn. Since there is no filtering immediately after amplification, the spectrally ASE-affected light is fed to the second (counter-pumped) preamplifier. Due to the sufficient seed power of 1 mW, pump light is already depleted at a relatively short fiber length of 2.2 m (Fig. 3, second plot).

The pre-picking AOM1 not only divides the pulse repetition frequency by a maximum of 30, but also suppresses continuous-wave background as well as the accumulated ASE between the pulses (first temporal filter), thus ensuring a clean 150  $\mu\text{W}$  input emission to the third preamplifier. In addition, the double-pass configuration of the third preamplifier allows spectral filtering between forward and backward direction, which is realized by a spectral 0.5 nm wide FBG with  $\sim 90\%$  signal wavelength reflection (first spectral filter). As a consequence, at an optimal fiber length of 2.2 m, the ASE content is strongly attenuated (Fig. 3, third plot). It should be noted that the FBG is prepared with a fiber connector, making it technically easy to replace the FBG with an FBG at another wavelength.

To predict an appropriate fiber length of the main amplifier, the highest possible average output power to maintain a 100 W pulse peak power at the amplifier output must be considered. In addition, the main amplifier average output power must be high enough to compensate for the approx. 50% loss from the subsequent post-picking process of AOM2 (second temporal filter). Accordingly, a 1 ns pulse at 1 MHz pulse repetition frequency requires an average output power of 100 mW, while the main amplifier must generate 250 mW including loss and safety margin.

In order to prevent the occurrence of stimulated Brillouin scattering and to keep the influence of self-phase modulation low, generating peak powers well above 100 W is not intended. If the pulse duration is changed while maintaining 100 W pulse peaks, the required pulse energy changes and the average output power can be adjusted. The same applies to changing pulse repetition frequencies, which vary between 1 MHz and 100 kHz at this point. To realize this feature, the design comprises a single pump laser diode with a flexibly selectable current for pumping the main amplifier. Since the overall pump power is limited, longer pulses may only be realized with a lower pulse repetition frequency. The result of the simulation of the main amplifier for 300 mW launched pump power and 5 mW seed power is shown in Fig. 3, fourth plot. According to this simulation, optimum performance is achieved at a total fiber length of approx. 2.7 m. To reduce the ASE content induced by the main amplifier, a second temporal (post-picking AOM2) and spectral (interference) filter follows in the final design.

A reduction of pulse repetition frequencies at MHz-level is difficult to achieve for Pockels cells due to piezoelectric ringing [28]. Instead, the use of an AOM as picking element and temporal filter can be advantageous for a number of reasons such as the superior suppression of zero-order diffracted radiation, fast switching and practical implementation of the low-voltage AOM driver electronics. Nevertheless, AOMs imprint two notable side effects onto the transmitted light. First, the center wavelength of the laser shifts by the amount of the RF driver frequency (Doppler effect), in this case 300 MHz. To work around this issue, both AOMs use inverse propagation directions of the traveling acoustic wave relative to the beam, resulting in a down-shifting and an up-shifting AOM. This neutralizes the AOM-induced frequency shifts, given that both AOMs are driven by the same RF-source. Second, an AOM gating signal of short duration can cause severe pulse-to-pulse power fluctuations, which is a consequence of the underlying physical principle: each pulse is diffracted by a moving acoustic compression wave packet generated from an electrical signal in the form of a 10 ns gated sinusoidal oscillation. Thus, at the given 300 MHz RF driver frequency, only about three side-dampened oscillations form the diffraction grating with a diffraction efficiency that depends strongly on the instantaneous phase of the acoustic wave packet at the time of pulse arrival. Consequently, each pulse is subject to a different phase and thus a different diffraction efficiency, which leads to the pulse-to-pulse fluctuations mentioned above. The described effect can be avoided if the pulse repetition frequency and the AOM driver signal are synchronized, which leads to a phase-locked state of the acoustic wave packet [29].

In the proposed setup, a pulse generator is used as a 3 MHz master clock, which sends two temporarily locked electrical signals. Firstly, a short ns-pulse of customized form to the EOIM (pulse shaping) and secondly, a symmetrical square pulse to the AOM control electronics (trigger). This trigger signal is processed in the AOM control electronics to generate three master clock synchronous signals, a sinusoidal 300 MHz carrier signal matched to the nominal AOM modulation frequency, and one gating signal for each AOM (Fig. 4). In principle, the gating signal is an electrical rectangular pulse of 10 ns duration by default (but adjustable), which can be delayed to temporally match the optical pulses. It also embodies the pulse picking mechanics, i.e. pre-picking AOM1 can divide pulse repetition frequency by 3–30 ( $\text{PRF} = 1 \text{ MHz} - 100 \text{ kHz}$ ), while post-picking AOM2 suppresses 3–60,000 pulses down to  $\text{PRF} = 50 \text{ Hz}$ . Both the gating signal and the 300 MHz carrier signal are mixed to form the AOM driver signal, which is then electronically amplified and sent to the corresponding AOM. In addition, the 300 MHz carrier signal can be phase-shifted relative to the gate signal to optimize diffraction efficiency of each AOM. It should be noted that both AOMs are water cooled to prevent thermal drift over time.

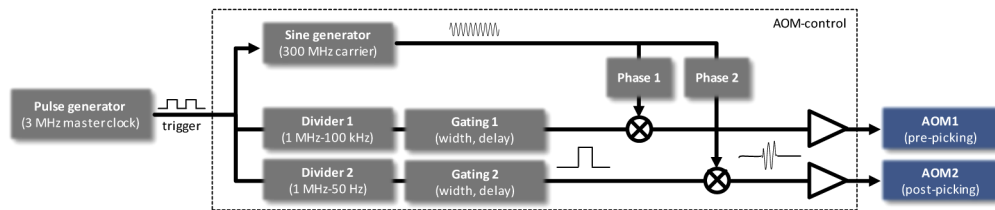


**Fig. 4.** Schematic representation of the synchronization between the optical pulse repetition frequency and the AOM driver signal to produce uniform pulse amplitudes after pulse picking.

#### 4. Experimental results

In general, one of the most important things about incremental amplification of low wavelengths in Yb-based fibers is to maintain control over the generated amplified spontaneous emission (ASE). For this reason, the discussion about the emergence and suppression of ASE is mandatory and will be treated first. Based on the amplifier design described above, the realized all-fiber setup contains a total of four fiber amplifier stages and four ASE suppression measures, two temporal filters (AOMs) and two spectral filters (FBG in preamplifier 3 and interference filter at the output).

The EOIM forms a 3 MHz nanosecond pulse train that propagates through preamplifiers 1 and 2 (Figs. 5(a) and 5(c), gray dotted lines). After passing through the pre-picking AOM1 (first temporal filter) and the FBG (first spectral filter) as part of preamplifier 3, the accumulated ASE can be reduced in its peak (around 1030 nm) either by 16 dB at 1 MHz (Fig. 5(a), blue line) or by 8 dB at 100 kHz pulse repetition frequency (Fig. 5(c), blue line). Additionally, the continuous-wave background power at 1010.6 nm, a remnant of the EOIM pulse shaping process, is removed. With the main amplification, ASE is once more increased by  $\sim 10$  dB, see Fig. 5(b) at 1 MHz and (d) at 100 kHz pulse repetition frequency (gray dotted lines). The output signal is further processed when passing through the post-picking AOM2 (second temporal filter) and an interference filter with 4 nm FWHM-bandwidth (second spectral filter). Figure 5(b) (red line) shows an 85 dB ASE suppression of the output emission at PRF = 1 MHz (116 mW of average power, derived pulse peak power 129 W, see Fig. 7(a)), which essentially corresponds to the maximum resolution of the optical spectrum analyzer (OSA) being used. At 1 kHz output pulse repetition frequency the average power of 110  $\mu$ W (120.5 W derived pulse peak power, see Fig. 7(b)) is too low to make use of the full dynamic range of the OSA. Thus a 65 dB ASE suppression can be verified experimentally (Fig. 5(d), red line), but according to the interference filter data sheet a significantly higher suppression ( $>100$  dB) is predicted at both repetition frequencies. A closer look at the spectrum reveals that the impact of self-phase modulation is negligible, since short fiber lengths were used, especially at the end of the system, where more powerful pulses are propagating. Hence, the spectrum of the output signal results only from the bandwidth-limited EOIM pulse shaping process.

Figure 6 shows the output power as a function of the pump power for pulse repetition frequencies of (a) 1 MHz and (b) 1 kHz. Regarding pump limitation, 1 MHz pulse repetition rate is the most demanding regime, but even then  $>100$  mW can be realized with single-mode pump laser diodes of moderate power. To address the pulse repetition frequency of 1 kHz, the main amplifier is operated at 100 kHz and only one of a hundred pulses passes the post-picking AOM2. When reducing the pulse repetition frequency from 100 kHz to 1 kHz, no reduction in peak power was observed for a photodiode signal, indicating that peak power remains stable at the various PRFs. The analysis of measured time traces reveals that there are no hidden pulses from the original 3 MHz pulse train, at least not above  $-40$  dBc, which is the maximum dynamic range of this



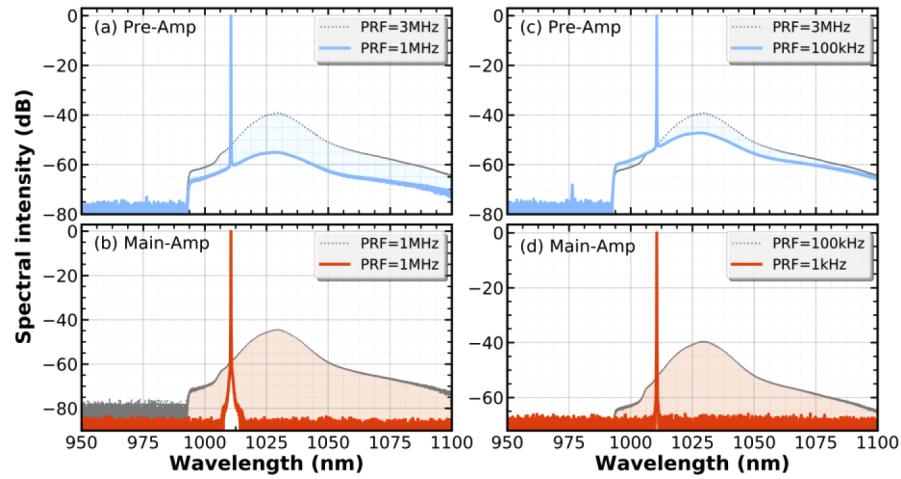


**Fig. 5.** Normalized measured spectra showing the emergence and suppression of ASE during propagation through preamplifier stages (blue lines) and main amplifier (red lines) with the high PRF mode (1 MHz at laser output) shown on the left side and the low PRF mode shown on the right side (1 kHz at laser output). (a) Comparison between the spectra at output preamplifier 2 (gray dotted line, PRF = 3 MHz) and at output preamplifier 3 after filtering via AOM1 and FBG (blue line, PRF = 1 MHz). (b) Comparison between the spectra at output main amplifier (gray dotted line, PRF = 1 MHz) and at the laser output after filtering via AOM2 and interference filter (red line, PRF = 1 MHz). (c) Comparison between the spectra at output preamplifier 2 (gray dotted line, PRF = 3 MHz) and at output preamplifier 3 after filtering via AOM1 and FBG (blue line, PRF = 100 kHz). (d) Comparison between the spectra at output main amplifier (gray dotted line, PRF = 100 kHz) and at the laser output after filtering via AOM2 and interference filter (red line, PRF = 1 kHz).

measurement. This is in accordance with the manufacturer's specifications, whereby each AOM should have an extinction ratio of  $>40$  dB, so the power content of residual intermediate pulses is negligible even at the lowest PRF.

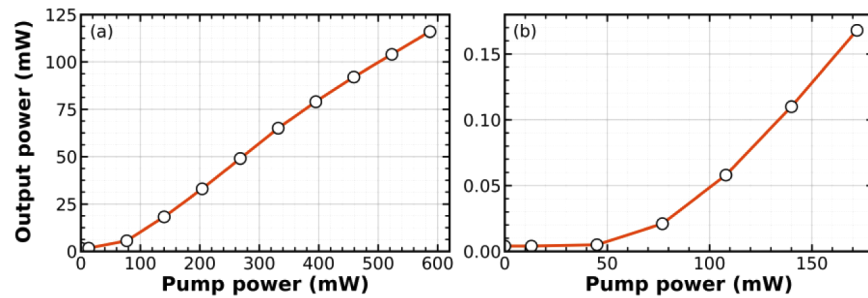


**Fig. 6.** Measured average output powers after post-picking AOM2 and filter at (a) PRF = 1 MHz and (b) PRF = 1 kHz versus the power of the main-amplifier pump laser diode.

In order to preclude potentially strong short-term pulse-to-pulse peak power fluctuations and to validate the synchronized AOM picking scheme for different pulse repetition frequencies, time traces were recorded on a photodiode and statistically evaluated (Fig. 7). The mean power value (red line) and the corresponding standard deviation (blue area) can be retrieved from each point in time ( $N = 100$  data records, 320 data points in time). By knowing the average output power,

the ASE content and the pulse repetition frequency, the photodiode signal can also be converted into a function of power over time. Around the  $>100$  W pulse peaks, the standard deviation is below 1%, which proves the correct function of the two PRF-synchronized AOMs. The jitter of the pulse duration is measured to be  $<10$  ps while the pulse-to-pulse jitter is determined by the master clock electronics ( $<25$  ps). The analysis of the backward-propagating light also shows that stimulated Brillouin scattering is not yet an issue. This was further confirmed by amplifying longer pulses with smaller bandwidth to an even higher peak power of  $>300$  W.

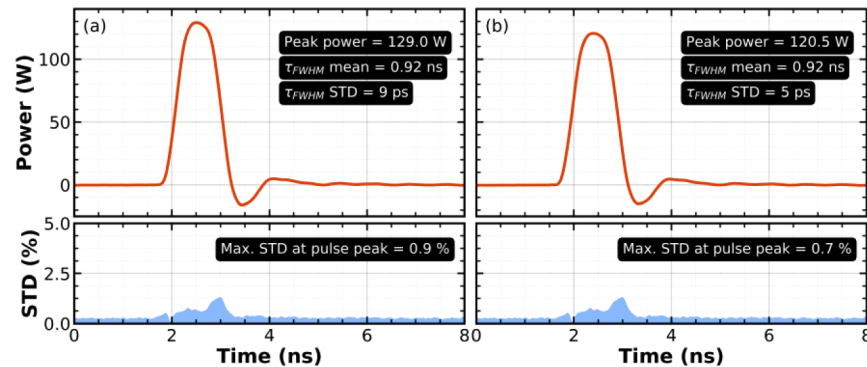


**Fig. 7.** Statistical analysis of 100 superimposed time traces at (a) 1 MHz and (b) 1 kHz pulse repetition frequency with mean value of power distribution (red line) and the corresponding standard deviation (blue) over time. In addition, values for the maximum peak power, the FWHM pulse duration (and its standard deviation) as well as the maximum standard deviation at the pulse peak are stated (black insets).

## 5. Summary

In conclusion, a four-stage Yb-doped fiber amplifier system was designed, simulated and realized to meet the requirements derived from an on-demand single-photon source experiment. Nanosecond pulses with arbitrary pulse shapes, adjustable pulse durations, pulse peak powers of  $>100$  W at flexible pulse repetition frequencies (0.05–1000 kHz) can be generated. The experimental results show that the amplifier system meets all application-related requirements at the most difficult wavelength of 1010.6 nm and that the measured laser pulse shape is consistent with the simulated pulse shape in Fig. 1(b). This was possible by implementing various measures, such as the use of different amplifier configurations, temporal and spectral filtering and the use of PRF-synchronized AOMs for pulse picking.

It should be formally noted that the single-photon generation experiment described in Section 2 needs three nanosecond-pulsed laser sources. The first (1010.6 nm) was comprehensively described in this paper (transition 2–3 in Fig. 1(a), orange). The second amplifier system for transition 3–4 in Fig. 1(a) (yellow) yields similar results, but is more efficient due to the complementary wavelength of 1018.6 nm, which is closer to the maximum gain of Yb-doped fibers. Both fiber amplifier systems (1010.6 nm and 1018.6 nm) are designed as rugged 19" rack systems and can be easily operated using the touch screen interface from which all relevant parameters are controlled. Transition 1–2 in Fig. 1(a) (dark blue) can be realized with a commercially available laser, since the power level is five orders of magnitude lower. The on-demand single-photon experiment is currently in preparation.

## Funding

European Regional Development Fund (2017 FGI 0014, EFRE-OP 2014-220); National Natural Science Foundation of China (61505099, 61975104).

## Disclosures

The authors declare no conflicts of interest.

## References

1. P. Benioff, "The computer as a physical system: A microscopic quantum mechanical Hamiltonian model of computers as represented by Turing machines," *J. Stat. Phys.* **22**(5), 563–591 (1980).
2. R. P. Feynman, "Simulating Physics with Computers," *Int. J. Theor. Phys.* **21**(6-7), 467–488 (1982).
3. F. Arute, K. Arya, R. Babbush, D. Bacon, J. C. Bardin, R. Barends, R. Biswas, S. Boixo, F. G. S. L. Brandao, D. A. Buell, B. Burkett, Y. Chen, Z. Chen, B. Chiaro, R. Collins, W. Courtney, A. Dunsworth, E. Farhi, B. Foxen, A. Fowler, C. Gidney, M. Giustina, R. Graff, K. Guerin, S. Habegger, M. P. Harrigan, M. J. Hartmann, A. Ho, M. Hoffmann, T. Huang, T. S. Humble, S. V. Isakov, E. Jeffrey, Z. Jiang, D. Kafri, K. Kechedzhi, J. Kelly, P. V. Klimov, S. Knysh, A. Korotkov, F. Kostritsa, D. Landhuis, M. Lindmark, E. Lucero, D. Lyakh, S. Mandrà, J. R. McClean, M. McEwen, A. Megrant, X. Mi, K. Michielsen, M. Mohseni, J. Mutus, O. Naaman, M. Neeley, C. Neill, M. Y. Niu, E. Ostby, A. Petukhov, J. C. Platt, C. Quintana, E. G. Rieffel, P. Roushan, N. C. Rubin, D. Sank, K. J. Satzinger, V. Smelyanskiy, K. J. Sung, M. D. Trevithick, A. Vainsencher, B. Villalonga, T. White, Z. J. Yao, P. Yeh, A. Zalcman, H. Neven, and J. M. Martinis, "Quantum supremacy using a programmable superconducting processor," *Nature* **574**(7779), 505–510 (2019).
4. E. Pednault, J. Gunnels, D. Maslov, and J. Gambetta, "On "Quantum Supremacy"," IBM Research Blog: Quantum computing (10/21/2019).
5. C. Ospelkaus, U. Warring, Y. Colombe, K. R. Brown, J. M. Amini, D. Leibfried, and D. J. Wineland, "Microwave quantum logic gates for trapped ions," *Nature* **476**(7359), 181–184 (2011).
6. E. Knill, R. Laflamme, and G. J. Milburn, "A scheme for efficient quantum computation with linear optics," *Nature* **409**(6816), 46–52 (2001).
7. J. L. O'Brien, "Optical Quantum Computing," *Science* **318**(5856), 1567–1570 (2007).
8. M. Tillmann, B. Dakic, R. Heilmann, S. Nolte, A. Szameit, and P. Walther, "Experimental boson sampling," *Nat. Photonics* **7**(7), 540–544 (2013).
9. S. Gasparoni, J.-W. Pan, P. Walther, T. Rudolph, and A. Zeilinger, "Realization of a photonic controlled-NOT gate sufficient for quantum computation," *Phys. Rev. Lett.* **93**(2), 020504 (2004).
10. I. Aharonovich, D. Englund, and M. Toth, "Solid-state single-photon emitters," *Nat. Photonics* **10**(10), 631–641 (2016).
11. P. Michler, A. Imamoglu, M. D. Mason, P. J. Carson, G. F. Strouse, and S. K. Buratto, "Quantum correlation among photons from a single quantum dot at room temperature," *Nature* **406**(6799), 968–970 (2000).
12. B. Lounis and W. E. Moerner, "Single photons on demand from a single molecule at room temperature," *Nature* **407**(6803), 491–493 (2000).
13. N. Mizuochi, T. Makino, H. Kato, D. Takeuchi, M. Ogura, H. Okushi, M. Nothaft, P. Neumann, A. Gali, F. Jelezko, J. Wrachtrup, and S. Yamasaki, "Electrically driven single-photon source at room temperature in diamond," *Nat. Photonics* **6**(5), 299–303 (2012).
14. A. MacRae, T. Brannan, R. Achal, and A. I. Lvovsky, "Tomography of a High-Purity Narrowband Photon from a Transient Atomic Collective Excitation," *Phys. Rev. Lett.* **109**(3), 033601 (2012).
15. L.-M. Duan, M. D. Lukin, J. I. Cirac, and P. Zoller, "Long-distance quantum communication with atomic ensembles and linear optics," *Nature* **414**(6862), 413–418 (2001).
16. F. Ripka, H. Kübler, R. Löw, and T. Pfau, "A room-temperature single-photon source based on strongly interacting Rydberg atoms," *Science* **362**(6413), 446–449 (2018).
17. M. D. Lukin, M. Fleischhauer, R. Cote, L. M. Duan, D. Jaksch, J. I. Cirac, and P. Zoller, "Dipole Blockade and Quantum Information Processing in Mesoscopic Atomic Ensembles," *Phys. Rev. Lett.* **87**(3), 037901 (2001).
18. M. M. Müller, A. Kölle, R. Löw, T. Pfau, T. Calarco, and S. Montangero, "Room-temperature Rydberg single-photon source," *Phys. Rev. A* **87**(5), 053412 (2013).
19. M. Saffman and T. G. Walker, "Creating single-atom and single-photon sources from entangled atomic ensembles," *Phys. Rev. A* **66**(6), 065403 (2002).
20. G. Lindblad, "On the Generators of Quantum Dynamical Semigroups," *Commun. Math. Phys.* **48**(2), 119–130 (1976).
21. F. Ripka, Y.-H. Chen, R. Löw, and T. Pfau, "Rydberg polaritons in a thermal vapor," *Phys. Rev. A* **93**(5), 053429 (2016).
22. A. Belz, "Viel-Wellen-Mischen zu Rydbergzuständen von thermischen Alkalidämpfen zur Anwendung in fortgeschrittener nichtlinearer Optik," Bachelor thesis, University of Stuttgart/PI5 (2018).

23. J. Limpert, F. Röser, S. Klingebiel, T. Schreiber, C. Wirth, T. Peschel, R. Eberhardt, and A. Tünnermann, "The Rising Power of Fiber Lasers and Amplifiers," *IEEE J. Sel. Top. Quantum Electron.* **13**(3), 537–545 (2007).
24. T. Eidam, S. Hanf, E. Seise, T. V. Andersen, T. Gabler, C. Wirth, T. Schreiber, J. Limpert, and A. Tünnermann, "Femtosecond fiber CPA system emitting 830 W average output power," *Opt. Lett.* **35**(2), 94–96 (2010).
25. T. Saule, S. Holzberger, O. de Vries, M. Plötner, J. Limpert, A. Tünnermann, and I. Pupeza, "Phase-stable, multi- $\mu$ J femtosecond pulses from a repetition-rate tunable Ti:Sa-oscillator-seeded Yb-fiber amplifier," *Appl. Phys. B* **123**(1), 17 (2017).
26. F. Beier, H.-J. Otto, C. Jauregui, O. de Vries, T. Schreiber, J. Limpert, R. Eberhardt, and A. Tünnermann, "2014 nm continuous-wave ytterbium-doped fiber amplifier emitting 146 W," *Opt. Lett.* **39**(13), 3725–3727 (2014).
27. [www.fiberdesk.com](http://www.fiberdesk.com)
28. G. D. Goodno, Z. Guo, R. J. D. Miller, I. J. Miller, J. W. Montgomery, S. R. Adhav, and R. S. Adhav, "Investigation of  $\beta$ -BaB<sub>2</sub>O<sub>4</sub> as a Q-switch for high power applications," *Appl. Phys. Lett.* **66**(13), 1575–1577 (1995).
29. O. de Vries, T. Saule, M. Plötner, F. Lücking, T. Eidam, A. Hoffmann, A. Klenke, S. Hädrich, J. Limpert, S. Holzberger, T. Schreiber, R. Eberhardt, I. Pupeza, and A. Tünnermann, "Acousto-optic pulse picking scheme with carrier-frequency-to-pulse-repetition-rate synchronization," *Opt. Express* **23**(15), 19586–19595 (2015).